

Unsupervised Light Field Depth Estimation via Multi-view Feature Matching with Occlusion Prediction

Shansi Zhang, Nan Meng and Edmund Y. Lam

Abstract—Depth estimation from light field (LF) images is a fundamental step for some applications. Recently, learning-based methods have achieved higher accuracy and efficiency than the traditional methods. However, it is costly to obtain sufficient depth labels for supervised training. In this paper, we propose an unsupervised framework to estimate depth from LF images. First, we design a disparity estimation network (DispNet) with a coarse-to-fine structure to predict disparity maps from different view combinations by performing multi-view feature matching to learn the correspondences more effectively. As occlusions may cause the violation of photo-consistency, we design an occlusion prediction network (OccNet) to predict the occlusion maps, which are used as the element-wise weights of photometric loss to solve the occlusion issue and assist the disparity learning. With the disparity maps estimated by multiple input combinations, we propose a disparity fusion strategy based on the estimated errors with effective occlusion handling to obtain the final disparity map. Experimental results demonstrate that our method achieves superior performance on both the dense and sparse LF images, and also has better generalization ability to the real-world LF images.

Index Terms—Light field, unsupervised depth estimation, feature matching, occlusion prediction.

I. INTRODUCTION

A light field (LF) camera has the ability of capturing both the intensities and directions of the light rays [1]–[3], to obtain LF images with multiple sub-aperture images (SAIs), each of which provides one viewpoint of the scene. As LF images contain rich geometric information, useful clues are available for depth (disparity) estimation. Usually, depth estimation is an essential step for some LF applications, such as 3D scene reconstruction [4], [5] and novel view synthesis [6]–[8]. However, the baseline between the adjacent SAIs is very narrow, which brings challenges for estimating depth from the LF images.

Traditional methods for LF depth estimation mainly follow two approaches. The first approach is to explore the structure of epipolar-plane images (EPIs) [9]–[12], where the pixels corresponding to the same scene point in different SAIs form a line with a slope proportional to the disparity value. Another approach focuses on the classical stereo matching to find the corresponding pixels among different SAIs [13]–[16]. However, EPI-based methods are mainly applicable to the densely sampled LF images, and the traditional stereo matching methods usually suffer from heavy computational costs. Recently, many learning-based methods [17]–[22] have

been proposed for LF depth estimation with improved accuracy and efficiency. They use deep neural networks to represent the estimators by learning from the depth labels. However, it is costly to acquire sufficient accurate depth labels, especially for the real-world LF images. Accordingly, those supervised methods are usually trained on the synthetic LF images, which often leads to performance degradation when generalizing to the real-world scenes.

To overcome the disadvantages of the traditional and supervised learning-based methods, we propose an unsupervised LF depth estimation framework by fully exploiting the LF geometry without using any ground truth. Usually, the unsupervised learning for depth [23]–[25] is based on the photo-consistency assumption that the pixels from different views corresponding to the same scene point are expected to have the same photometric values. To better utilize this assumption, we design a disparity estimation network that explicitly performs multi-view feature matching to learn the correspondences among different views. Moreover, occlusion is a challenging issue in LF depth estimation, which leads to the violation of photo-consistency. Thus, we introduce an occlusion prediction network to eliminate the adverse impact of occlusions and assist the learning of disparity estimation. The main contributions of our work are as follows:

- We design a DispNet, which takes as inputs multiple view combinations with different distances. It performs multi-view feature matching by constructing memory-efficient cost volumes, and adopts a coarse-to-fine structure, which consists of two branches with shared modules to estimate the coarse and residual disparity maps, respectively.
- We design an OccNet for occlusion prediction, which is trained through the reconstruction of the central view. The predicted occlusion maps are used as the element-wise weights of the photometric loss to mitigate the effect of occlusions during disparity learning, without introducing extra computational cost during inference.
- We propose a multi-disparity fusion strategy to merge the disparity maps estimated by different input combinations. Occlusions are handled effectively when deriving the error maps with the diagonal views, and several fusion approaches are explored to obtain the final disparity map.

Extensive experiments have been conducted, which demonstrates that our method achieves superior performance on both the dense and sparse LF images, and presents better generalization ability to the real-world LF images compared with the other state-of-the-art competitors.

II. RELATED WORK

The existing methods for LF depth are reviewed in terms of two types, i.e., traditional methods and learning-based

S. Zhang and E.Y. Lam are with the Department of Electrical and Electronic Engineering, The University of Hong Kong, Pokfulam, Hong Kong e-mail: sszhang@eee.hku.hk, elam@eee.hku.hk.

N. Meng is with the Li Ka Shing Faculty of Medicine, The University of Hong Kong, Pokfulam, Hong Kong.

methods.

A. Traditional methods

Traditional methods for LF depth estimation mainly focus on the EPI structure and stereo matching. For the EPI-based methods, Wanner and Goldluecke [9] estimated the disparity maps locally by using EPI analysis, which works fast without the expensive matching cost minimization. Zhang et al. [10] proposed a spinning parallelogram operator (SPO) to locate the lines in EPI and calculate their slopes to acquire the depth information. Zhang et al. [11] exploited the line structure of EPI and locally linear embedding (LLE) to estimate the local depth by minimizing the matching cost. Sheng et al. [12] developed a strategy to extract EPIs in multiple directions besides the horizontal and vertical EPIs for calculating the local depth, which is combined with the predicted occlusion boundaries to obtain the final depth map.

For the stereo matching-based methods, Jeon et al. [13] constructed a cost volume to estimate the multi-view stereo correspondences, which was used to optimize the depths in weak texture regions. Then, the local depth map was refined iteratively by fitting the local quadratic function to yield the final depth map. Tao et al. [14] utilized the shading information to improve the local shape estimation from defocus and correspondence and developed a framework that exploits LF angular coherence for depth and shading optimization. Lee et al. [15] computed binary maps through foreground-background separation to obtain the disparity maps. Huang et al. [16] proposed a stereo matching algorithm using an empirical Bayesian framework, which employs the pseudo-random field to explore the statistical cues of LF.

Occlusion issue is often encountered in LF depth estimation since the photo-consistency assumption does not hold in the occlusion regions. There are some methods designed to handle this issue. Wang et al. [26] found that photo-consistency still holds in about half of the views when occlusions exist, and they predicted the occlusions, which was used as a regularizer to improve depth estimation. Williem et al. [27] focused on the robust depth estimation from noisy LF with occlusions. They introduced two data costs with angular entropy metric and adaptive defocus response to handle the occlusions and noises. Chen et al. [28] proposed a method with partially occluded region detection through super-pixel regularization and showed that even a simple least square model can achieve superior depth estimation after manipulating the label confidence and edge strength.

These traditional methods usually involve complex optimization and long execution time, and can not achieve a good trade-off between the accuracy and efficiency.

B. Learning-based methods

The recent researches on LF depth estimation mainly focus on the learning-based methods, which can usually achieve higher accuracy and inference speed. Most existing learning-based methods adopt supervised training using depth labels. Sun et al. [17] developed a convolutional neural network (CNN) to estimate LF disparity by extracting enhanced EPI

features. Heber et al. [18] proposed a U-shaped network to extract geometric information from LF, with 3D convolutional layers to examine the EPI volumes for robust depth prediction. Shin et al. [19] developed a CNN framework by taking as input the views from different angular dimensions. They also proposed some data augmentation methods for LF to overcome the deficiency of training data. Shi et al. [20] proposed a framework for learning depth from the dense and sparse LF images with three steps, including initial depth estimation by a fine-tuned FlowNet 2.0 [29], occlusion-aware depth fusion and refinement by another network. Tsai et al. [21] proposed a view selection network by learning an attention map to estimate the contribution of each view on depth. The attention map was constrained to be symmetric in accordance with the LF views. Chen et al. [22] developed a multi-level fusion network with attention, which contains four branches to perform intra-branch and inter-branch fusion, to select the features that can provide more useful information for depth. These supervised methods heavily rely on the labeled data, and their performance may be degraded when the labeled data is limited.

Unsupervised methods can overcome the reliance on the labeled data. Srinivasan et al. [30] synthesized 4D LF from a single 2D image with CNN, and unsupervised single image depth estimation was incorporated within their pipeline. Peng et al. [31] proposed an unsupervised CNN framework by designing a combined loss with compliance and divergence constraints to estimate LF disparity. Zhou et al. [32] developed an unsupervised monocular LF depth network, which was trained by the improved photometric losses and taking only one view as input. Jin et al. [33] proposed an unsupervised occlusion-aware framework by exploring the angular coherence among different LF subsets. The above unsupervised methods leverage the photometric signal as the implicit supervision, but their performances still have obvious gaps with the supervised methods.

III. PROPOSED METHOD

We first describe our overall framework for LF disparity estimation in Sec. III-A. Then, we introduce the architecture of our DispNet in Sec. III-B, the occlusion prediction method in Sec. III-C, and the loss functions for training in Sec. III-D. Finally, we introduce our disparity fusion strategy in Sec III-E.

A. Overall framework

A 4D LF image is represented as $L(u, v, x, y) \in \mathbb{R}^{U \times V \times X \times Y}$, with the angular dimension (u, v) and the spatial dimension (x, y) . It consists of $U \times V$ SAls, each of which records the scene from one viewpoint, with a spatial resolution of $X \times Y$. Our target is to estimate the disparity map of the central view relative to its adjacent views. According to the LF geometry, the relationship between the central view and any other view in terms of the central disparity $d(x, y)$ is expressed as

$$L(u_c, v_c, x, y) = L(u, v, x + d(x, y) \cdot (u_c - u), y + d(x, y) \cdot (v_c - v)), \quad (1)$$

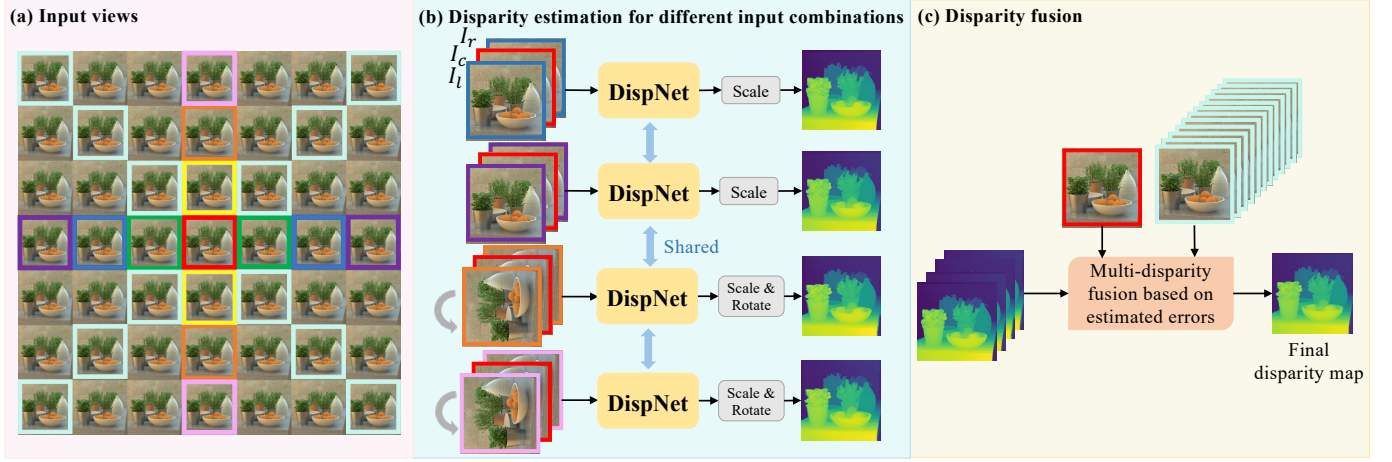


Fig. 1. (a) The views input to the DispNet and used for fusion. (b) The DispNet takes as inputs the central view I_c , the left source view I_l and the right source view I_r . The views from the same column are rotated by 90° . Multiple disparity maps (after scaling and rotation) are obtained from different input combinations. (c) The estimated disparity maps are fused according to their estimated errors with the diagonal views to yield the final disparity map.

where (u_c, v_c) is the angular position of the central view.

The overall framework of our method is depicted in Fig. 1, which presents the complete inference process. Three views, including the central view I_c , the left source view I_l and the right source I_r view (“source” means that they are warped according to the disparity to reconstruct the central view), are fed to the DispNet. They are in the same row or column, and the two source views framed by the same color are located symmetrically to the central view. This input strategy can eliminate the ambiguity caused by the occlusions without incorporating any redundant inputs, since each scene point is usually visible in at least two views. For the given example of a 7×7 LF image (Fig. 1(a)), there are totally 6 input combinations. As the views from the same column have vertical disparities, they are rotated by 90° (counterclockwise) before being input to the network so that their disparities become horizontal, and the corresponding output disparity map needs to be rotated by -90° (clockwise) to recover the orientation. In this way, only horizontal disparity estimation is involved to make the learning easier. Multiple disparity maps are obtained from different input combinations by the shared DispNet, and they need to be scaled by the distance between the source views and central view. Using the nonadjacent views to estimate disparity can help to alleviate the inaccurate estimation caused by the narrow LF baseline. Then, these disparity maps are fused based on their estimated errors using the diagonal views to obtain the final disparity map. In what follows, we will introduce each part in detail.

B. Disparity estimation

The architecture of our DispNet is shown in Fig. 2(a). The central view I_c and the two source views I_l and I_r are fed to a shared feature extractor. The feature extractor (Fig. 2(b)) consists of several residual blocks, each of which has two 3×3 convolution layers with leaky Rectified Linear Unit (ReLU) activation, and the atrous spatial pyramid pooling (ASPP) [34] for encoding multi-scale features, which contains three 3×3

convolutions with dilation rates of 3, 6 and 8 respectively, and a global average pooling (GAP) followed by a 1×1 convolution.

The extracted features of the three views are used to construct the cost volumes through feature matching. The detailed procedures of constructing the coarse cost volume is illustrated in Fig. 3. First, we prescribe D disparity samples with the maximum value s_{\max} and the interval $\Delta s = \frac{2s_{\max}}{D-1}$, and express them in a vector form, with $\mathbf{s} = [-s_{\max}, -s_{\max} + \Delta s, -s_{\max} + 2\Delta s, \dots, s_{\max}]^T$. Given the features of the three views with the size of $C \times H \times W$, the left and right source features are warped to match with the reference (central) features by a disparity sample s_i from \mathbf{s} . Then, the variance of the warped features and reference features is calculated to measure their difference, which is treated as the matching cost at disparity sample s_i (accurate disparity for each pixel leads to a small variance). The cost volume is obtained by concatenating the matching costs at all the disparity samples, with a size of $C \times D \times H \times W$. Compared with the construction approaches in stereo matching [35], [36], the variance-based feature matching is much more memory-efficient and can also adapt to any number of input views without increasing the size of cost volume.

The coarse cost volume is further processed by the 3D cost filters, each of which consists of several 3D residual blocks with skip connections to fuse the features in different levels (Fig. 2(c)), to yield the cost \mathbf{c}_{coa} with a size of $D \times H \times W$. Then, we employ the disparity regression method proposed in [37] to derive the coarse disparity map \tilde{d}_{coa} , with

$$\tilde{d}_{\text{coa}}(x, y) = \mathbf{s} \cdot \text{softmax}(\mathbf{c}_{\text{coa}}(x, y)), \quad (2)$$

where $\text{softmax}(\cdot)$ is the softmax function to obtain the probability of each disparity sample, and \cdot means the inner product.

To further refine the disparity map, a residual cost volume is constructed by using the same extracted features. Similarly, we set a residual sample vector $\mathbf{s}' = [-s'_{\max}, -s'_{\max} + \Delta s', -s'_{\max} + 2\Delta s', \dots, s'_{\max}]^T$ with a size of D' , the max-

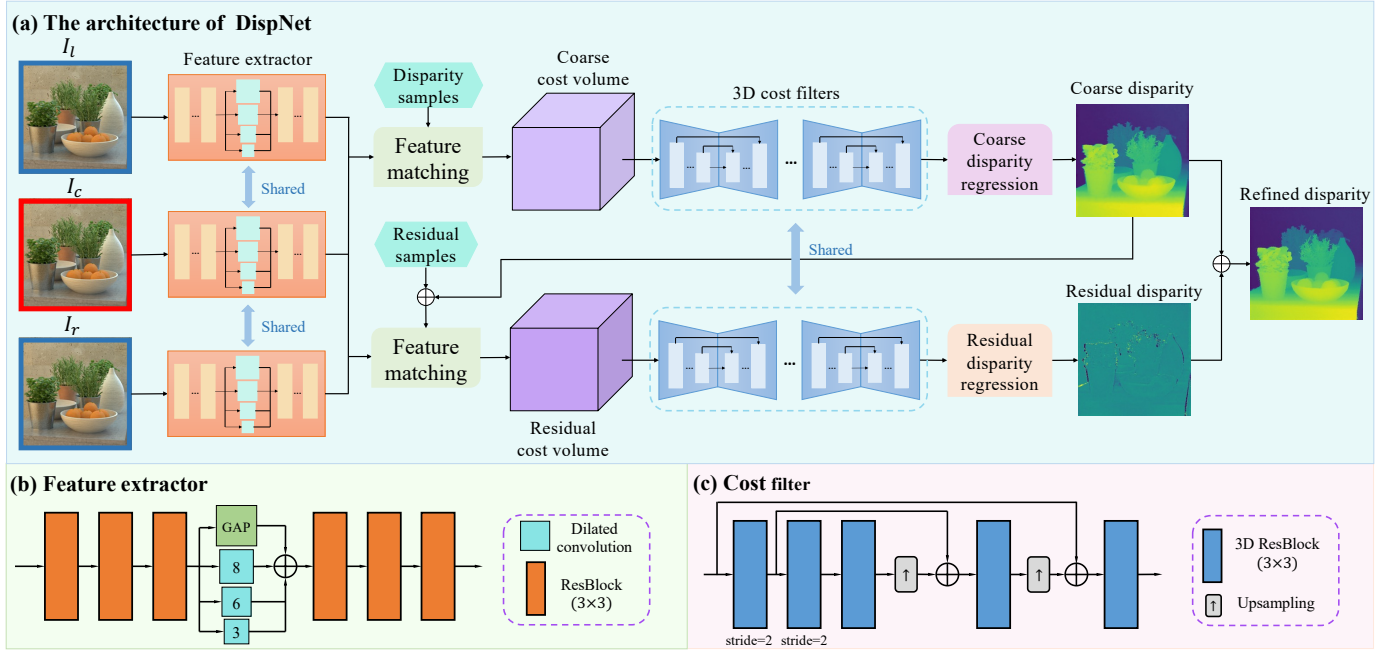


Fig. 2. (a) The DispNet consists of two branches with shared feature extractor and 3D cost filters to estimate the coarse disparity map and residual map by constructing the coarse and residual cost volumes. The coarse disparity map and residual map are added to obtain the refined disparity map. (b) The feature extractor consists of several residual blocks and the ASPP module. (c) The cost filter consists of several 3D residual blocks with skip connections.

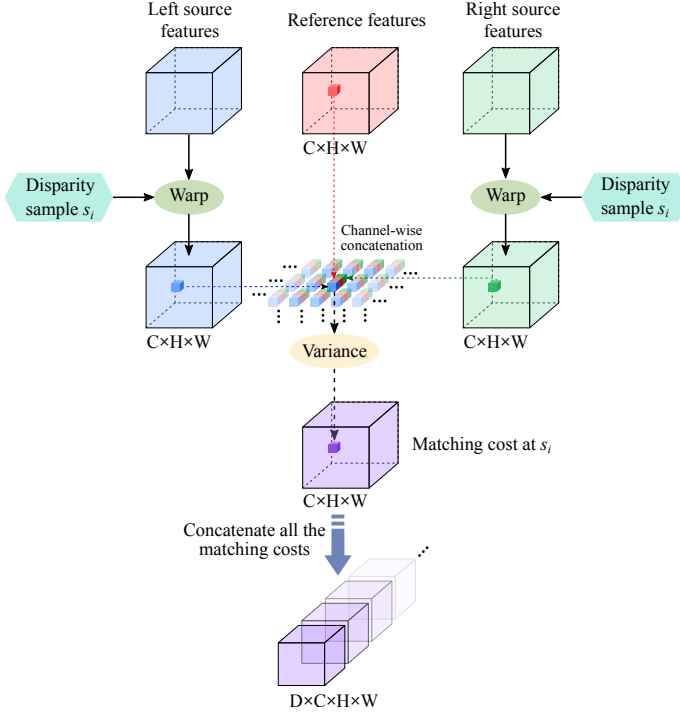


Fig. 3. The left and right source features are warped according to a disparity sample s_i to match with the reference features. The variance of the warped features and reference features is calculated to yield the matching cost at disparity sample s_i . The final cost volume is obtained by concatenating the matching costs at all the disparity samples.

The left and right source features are warped according to the coarse disparity map and a residual sample s'_i from s' , with a new disparity sample $\tilde{d}_{\text{coa}}(x, y) + s'_i$ at each position to match with the reference features. The interval of residual sampling is much smaller than that of coarse sampling in order to improve the disparity accuracy. The matching cost at each residual sample is derived by calculating the variance of the warped and reference features, and the residual cost volume is obtained by concatenating the matching costs at all the residual samples. Then, the residual cost volume is processed by the shared cost filters to yield the residual cost \mathbf{c}_{res} with a size of $D' \times H \times W$, which is used to derive the residual map \tilde{d}_{res} , with

$$\tilde{d}_{\text{res}}(x, y) = \mathbf{s}' \cdot \text{softmax}(\mathbf{c}_{\text{res}}(x, y)). \quad (3)$$

Thus, the refined disparity map \tilde{d} is obtained by

$$\tilde{d}(x, y) = \tilde{d}_{\text{coa}}(x, y) + \tilde{d}_{\text{res}}(x, y). \quad (4)$$

When the input views are not adjacent, the output disparity maps from DispNet need to be scaled according to the view distance. In addition, the disparity maps predicted by the views on the same column need to be rotated by -90° to recover the orientation. Thus, the estimated central disparity map \hat{d} is obtained by

$$\hat{d}(x, y) = \frac{\tilde{d}(x, y)}{u_c - u_l}, \quad (5)$$

if the input views are from the same row, or

$$\hat{d}(x, y) = \text{rot}_{-90^\circ} \left(\frac{\tilde{d}(x, y)}{v_c - v_l} \right), \quad (6)$$

imum residual sample s'_{max} , and the interval $\Delta s' = \frac{2s'_{\text{max}}}{D'-1}$.

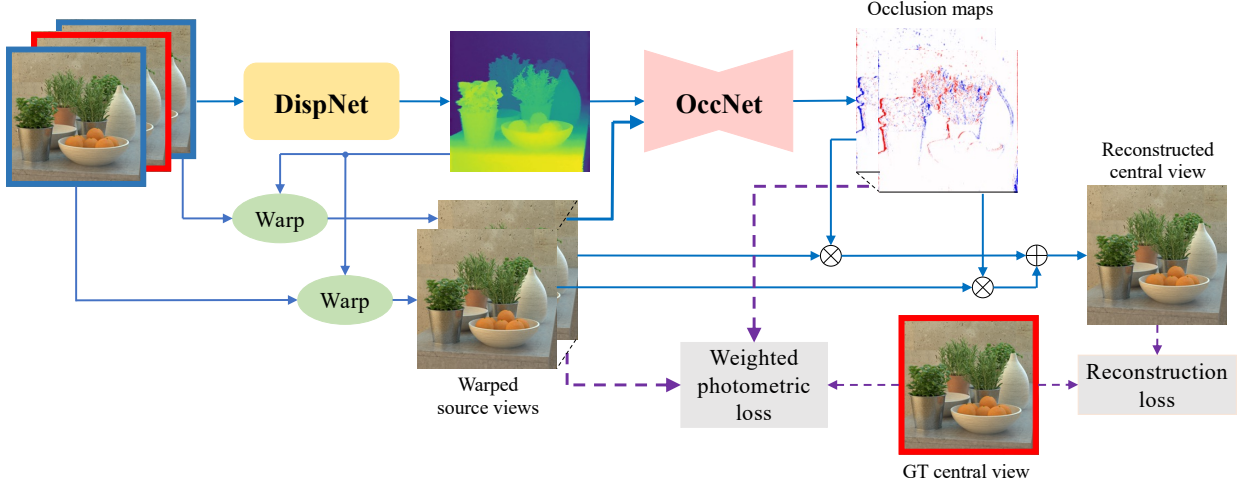


Fig. 4. The estimated disparity map from the DispNet is used to warp the two source views to the central view. Then, the concatenation of the warped views and the disparity map is input to the OccNet to predict the occlusion maps, which are used as the pixel-wise weights of the photometric loss, and also the confidence maps for reconstructing the central view. The OccNet is trained through the reconstruction loss between the two warped views and the central view.

if the input views are from the same column, where u_l and v_l are the angular coordinates of the left source view, and rot_{-90° means rotating by -90° .

C. Occlusion prediction

During training, \tilde{d} is used to warp the left and right source views to the central view, yielding $I_{l \rightarrow c}$ and $I_{r \rightarrow c}$, with

$$I_{l \rightarrow c}(x, y) = I_l(x + \tilde{d}(x, y), y), \quad (7)$$

$$I_{r \rightarrow c}(x, y) = I_r(x - \tilde{d}(x, y), y). \quad (8)$$

We introduce an OccNet to predict the occlusion regions for the two source views, which takes the concatenation of $I_{l \rightarrow c}$, $I_{r \rightarrow c}$ and \tilde{d} as inputs, as shown in Fig. 4. The OccNet adopts an encoder-decoder architecture with residual blocks and skip connections operating on multi-scale features. A softmax activation is used in the last convolution layer to output the occlusion maps, O_l and O_r for $I_{l \rightarrow c}$ and $I_{r \rightarrow c}$, respectively. The occlusion maps are used as the pixel-wise weights of the photometric loss for training the DispNet, and also treated as the confidence maps of the two warped views for reconstructing the central view, since the occlusion regions usually result in larger warping errors, and therefore less confidence for the reconstruction. The reconstructed central view I_{rec} by the two warped views and their corresponding occlusion maps is expressed as

$$I_{\text{rec}} = O_l \odot I_{l \rightarrow c} + O_r \odot I_{r \rightarrow c}, \quad (9)$$

where \odot represents the element-wise multiplication, and $O_l(x, y) + O_r(x, y) = 1$.

The OccNet is only employed during training to solve the occlusion issue, and does not influence the inference efficiency.

D. Loss function

According to the photo-consistency assumption, the difference between the warped views and central view should be

as small as possible. However, photo-consistency is violated in the occlusion regions, which causes inaccurate photometric loss and therefore impairs the network training. It is expected that the weights of photometric loss in the occlusion regions are lower. Thus, the occlusion maps from OccNet can be used as the element-wise weights to derive the weighted photometric loss, with

$$\begin{aligned} \ell_{\text{wpm}} = & \frac{1}{N} \sum_{x,y} O_l(x, y) |I_{l \rightarrow c}(x, y) - I_c(x, y)| \\ & + \frac{1}{N} \sum_{x,y} O_r(x, y) |I_{r \rightarrow c}(x, y) - I_c(x, y)|, \end{aligned} \quad (10)$$

where N is the total number of pixels in each view.

To better constrain the consistency between the warped views and central view, we employ the structural similarity (SSIM) [38] loss, expressed as

$$\ell_{\text{SSIM}} = 1 - \frac{\text{SSIM}(I_{l \rightarrow c}, I_c) + \text{SSIM}(I_{r \rightarrow c}, I_c)}{2}. \quad (11)$$

The OccNet is trained by the reconstruction loss, with

$$\ell_{\text{rec}} = \|I_{\text{rec}}(x, y) - I_c(x, y)\|_1, \quad (12)$$

where $\|\cdot\|_1$ is the ℓ_1 -norm operator.

To improve the smoothness of the estimated disparity map while preserving the boundary structures of the objects, we leverage the structure-aware smoothness loss [39], expressed as

$$\ell_{\text{sm}} = \frac{1}{N} \sum_{x,y} |\nabla \tilde{d}(x, y)| \times \exp(-\eta |\nabla I_c(x, y)|), \quad (13)$$

where ∇ means calculating the gradients along both the horizontal and vertical directions, and η is a hyperparameter for structure awareness [40].

Moreover, we also introduce a similar smoothness loss for the occlusion map, written as

$$\ell_{\text{sm-occ}} = \frac{1}{N} \sum_{x,y} |\nabla O_l(x, y)| \times \exp(-\eta |\nabla I_c(x, y)|), \quad (14)$$

which is only applied to O_l since $O_r(x, y) = 1 - O_l(x, y)$.

The DispNet and OccNet are trained simultaneously by the following full loss, with

$$\ell_{\text{full}} = \ell_{\text{wpm}} + \ell_{\text{rec}} + \alpha_1 \ell_{\text{SSIM}} + \alpha_2 \ell_{\text{sm}} + \alpha_3 \ell_{\text{sm-occ}}, \quad (15)$$

where ℓ_{wpm} and ℓ_{rec} are the necessary losses, and the others are the auxiliary losses with coefficients $\alpha_1 \sim \alpha_3$. It should be noted that these loss terms are also applied to the coarse disparity map \tilde{d}_{coa} , but we omit those procedures for simplicity.

E. Multi-disparity fusion based on estimated errors

Multiple disparity maps can be obtained by the DispNet with different input combinations. To obtain the final disparity map, we propose a disparity fusion strategy to merge these disparity maps by selecting more accurate pixels from each disparity map.

Suppose that we have n estimated disparity maps $\{\hat{d}_j\}_{j=1}^n$, and m diagonal views for verification. With each disparity map, the diagonal views are warped to the central view, and the warping errors are calculated. However, some of the warping errors are not accurate due to the occlusions. If occlusions are involved when warping some of the diagonal views to the central view, their warping errors at the corresponding positions would be large, which results in large variances among the m warping errors. Thus, we calculate the standard deviation of the warping errors to judge if occlusions exist at each position, and obtain a binary mask.

Here, we define $\epsilon_j(x, y, z)$ as the warping error maps of the m diagonal views using the disparity map \hat{d}_j , with a size of $H \times W \times m$, and $\sigma_z(\cdot)$ as the standard deviation along the z dimension. Then the binary mask M_j is formulated as

$$M_j(x, y) = \begin{cases} 1 & \sigma_z(\epsilon_j(x, y, z)) > \theta \\ 0 & \text{otherwise} \end{cases} \quad (16)$$

where θ is the threshold to judge occlusions, which is scene-dependent and determined according to the mean of the standard deviations along the x and y dimension.

If occlusions exist at a position (x, y) , we use the median value of the warping errors to represent its estimated error, which can eliminate the influence of large warping errors due to occlusions. If there is no occlusion, its estimated error is represented by the mean of all the warping errors. The concrete procedure is expressed as

$$\epsilon_j^{\text{occ}}(x, y) = \text{median}_z(\epsilon_j(x, y, z)), \quad (17)$$

$$\epsilon_j^{\text{nocc}}(x, y) = \text{mean}_z(\epsilon_j(x, y, z)), \quad (18)$$

where ϵ_j^{occ} and ϵ_j^{nocc} represent the estimated errors in the occlusion and non-occlusion regions, respectively, $\text{median}_z(\cdot)$ and $\text{mean}_z(\cdot)$ denote the median and mean values along the z dimension. Then, the estimated error map ϵ_j^{est} for \hat{d}_j is obtained by

$$\epsilon_j^{\text{est}} = M_j \odot \epsilon_j^{\text{occ}} + (1 - M_j) \odot \epsilon_j^{\text{nocc}}. \quad (19)$$

With the above procedures, we can derive the error maps $\{\epsilon_j^{\text{est}}\}_{j=1}^n$ for all the disparity maps. Next, we need to merge

these disparity maps according to their estimated errors. Here, we consider several different fusion approaches. The first one is the minimum error fusion by choosing the pixels with the minimum errors from each disparity map, and the final disparity map \hat{d}_{final} is derived by

$$j' = \arg \min_j (\epsilon_j^{\text{est}}(x, y)), \\ \hat{d}_{\text{final}}(x, y) = \hat{d}_{j'}(x, y). \quad (20)$$

The second approach is the weighted fusion, where the weights are obtained by the softmax function and negatively correlated with the errors. Moreover, we can choose different numbers of disparity pixels for weighted fusion at each position. If n' ($n' \leq n$) disparity pixels with the smallest errors are used at each position, the final disparity map is obtained by

$$\mathbf{w}(x, y) = \text{softmax}(-\epsilon^{\text{est}}(x, y)), \quad (21)$$

$$\hat{d}_{\text{final}}(x, y) = \sum_{j=1}^{n'} w_j(x, y) \times \hat{d}_j(x, y), \quad (22)$$

where $\epsilon^{\text{est}}(x, y) = \{\epsilon_j^{\text{est}}(x, y)\}_{j=1}^{n'}$ denotes the smallest n' errors at position (x, y) , and $\mathbf{w}(x, y) = \{w_j(x, y)\}_{j=1}^{n'}$ denotes their corresponding weights.

IV. EXPERIMENTS

A. Datasets

To evaluate the performance more comprehensively, we used both the synthetic and real-world LF datasets. The synthetic LF datasets include both the densely and sparsely sampled LF images. The synthetic dense LF images are from the HCI dataset [41] and DLF dataset [20], with a disparity range $[-4, 4]$ pixels between the adjacent views. The synthetic sparse LF images are from the SLF dataset [20], with a much larger disparity range $[-20, 20]$ pixels. The real-world LF images are from the Stanford Lytro LF Archive [42], Kalantari [43] and EPFL LF [44] datasets. They can also be treated as dense LFs since their disparities are very small. For all the LF images, the central 7×7 SAIs were used to estimate the disparity maps for the central views.

B. Implementation details

For the DispNet, the number of cost filters is set to 3, and the maximum channel number within the feature extractor is 128. The disparity range for the dense LFs was set to $[-12, 12]$ (three times the disparity range between the adjacent views) with a coarse sampling interval 1, and the residual range was set to $[-1, 1]$ with a fine sampling interval 0.1. For the sparse LFs, only the central view and its adjacent views were used due to the limited memory resource for a large disparity range. Thus, the disparity range was set to $[-20, 20]$ with a coarse sampling interval 1.2, and the residual range was set to $[-2, 2]$ with a fine sampling interval 0.12. For the OccNet, the feature resolution within the encoder was gradually reduced to $\frac{1}{4}$ scale while the feature channels were increased from 16 to 64. The OccNet is very lightweight with only 0.113 M parameters,

TABLE I
EVALUATION ON THE HCI DATASET. **RED**: BEST AMONG ALL THE METHODS; **BLUE**: BEST AMONG THE UNSUPERVISED METHODS.

Methods		Dino				Sideboard			
		MSE ($\times 100$)	BPR (0.07)	BPR (0.03)	BPR (0.01)	MSE ($\times 100$)	BPR (0.07)	BPR (0.03)	BPR (0.01)
Supervised	EPINet [19]	0.167	1.286	3.452	22.401	0.742	4.277	10.824	37.999
	LFAAttNet [21]	0.093	0.848	2.340	12.224	0.531	2.870	7.243	20.739
Non-learning	OCC [26]	0.944	15.366	50.167	88.810	2.073	17.910	50.550	84.653
	FBS [15]	0.664	8.427	23.533	65.390	1.072	13.296	32.516	70.042
Unsupervised	UnCNN [31]	1.807	23.660	47.876	78.724	3.149	26.173	45.384	82.924
	UnMonocular [32]	1.031	5.402	14.757	43.258	2.770	10.947	23.646	61.406
	UnOCC [33]	0.63	8.25	-	-	1.79	14.20	-	-
	Ours	0.650	6.586	16.722	46.380	1.738	12.013	25.848	58.744
Methods		Backgammon				Pyramids			
		MSE ($\times 100$)	BPR (0.07)	BPR (0.03)	BPR (0.01)	MSE ($\times 100$)	BPR (0.07)	BPR (0.03)	BPR (0.01)
Supervised	EPINet [19]	3.629	3.580	6.289	20.899	0.008	0.192	0.913	11.876
	LFAAttNet [21]	3.648	3.126	3.984	11.582	0.004	0.195	0.489	2.063
Non-learning	OCC [26]	22.782	13.522	44.899	91.402	0.077	1.450	25.574	92.860
	FBS [15]	5.805	10.162	22.181	65.407	0.029	0.549	5.705	78.243
Unsupervised	UnCNN [31]	11.034	31.783	65.583	87.987	0.191	10.849	43.972	79.113
	UnMonocular [32]	11.833	12.311	28.524	68.312	0.027	0.262	8.725	35.594
	UnOCC [33]	6.684	14.371	-	-	0.213	7.348	-	-
	Ours	5.740	10.710	18.452	51.066	0.023	0.670	4.720	23.882

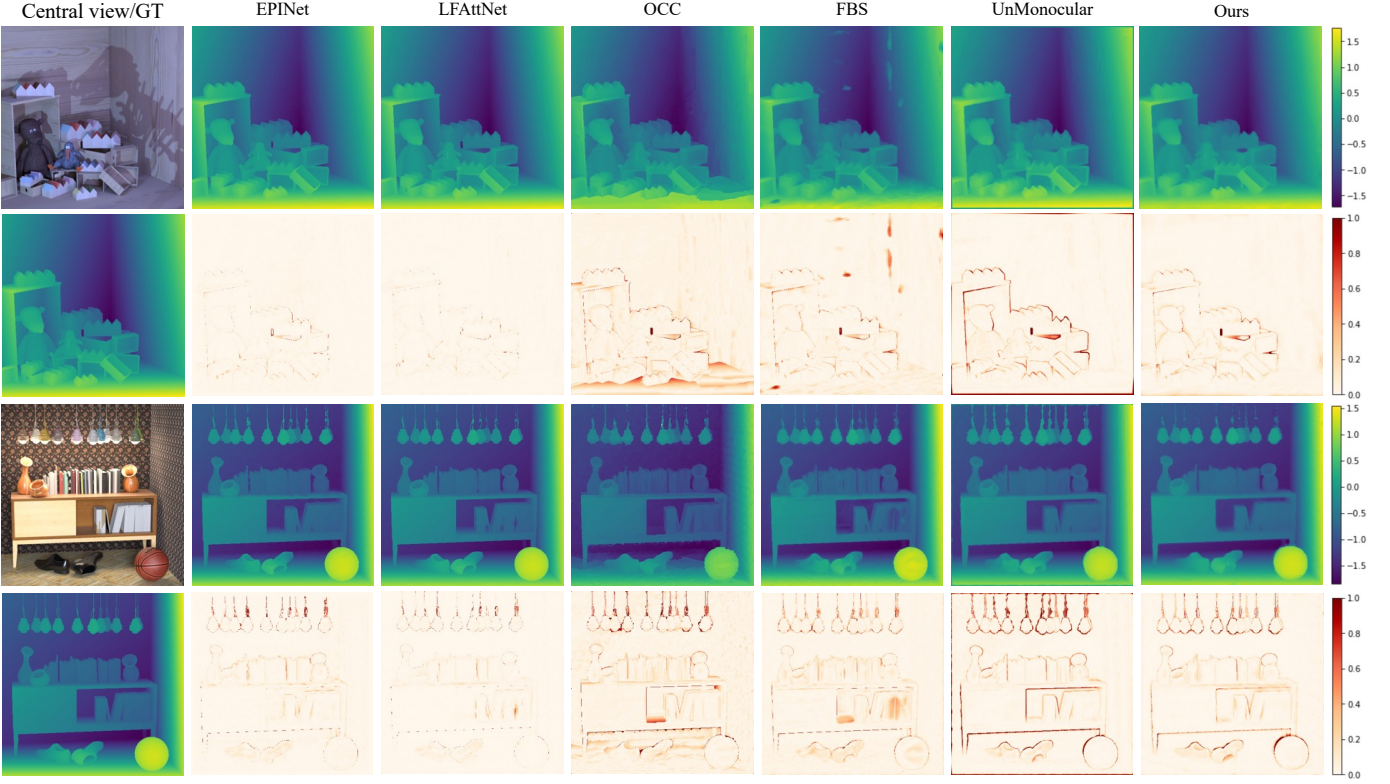


Fig. 5. Visual results of different methods on the scenes from the HCI dataset [41], with the error maps relative to the ground truths.

During training, all the views were cropped to 256×256 randomly. The initial learning rate was set to 1×10^{-3} and multiplied by 0.8 every 50 epochs. Moreover, we empirically set $\alpha_1 = 1$ for the SSIM loss, and $\eta = 100$, $\alpha_2 = 0.1$ and $\alpha_3 = 0.005$ for the smoothness losses. The DispNet and OccNet were jointly trained by the Adam optimizer [45] for about 500 epochs.

During inference, different view combinations were input to the DispNet to estimate multiple disparity maps. For the dense LFs, the input combinations (expressed by the angular

coordinates) are $[(u_c - 3, v_c), (u_c, v_c), (u_c + 3, v_c)]$, $[(u_c - 2, v_c), (u_c, v_c), (u_c + 2, v_c)]$, $[(u_c, v_c - 3), (u_c, v_c), (u_c, v_c + 3)]$, $[(u_c, v_c - 2), (u_c, v_c), (u_c, v_c + 2)]$, and the weighted fusion was adopted. For the sparse LFs, the input combinations are $[(u_c - 1, v_c), (u_c, v_c), (u_c + 1, v_c)]$, $[(u_c, v_c - 1), (u_c, v_c), (u_c, v_c + 1)]$, and the minimum error fusion was adopted as there are only two estimated disparity maps.

TABLE II
EVALUATION ON THE DLF DATASET. **RED**: BEST AMONG ALL THE METHODS; **BLUE**: BEST AMONG THE UNSUPERVISED METHODS.

Methods		Toys				Antiques			
		MSE ($\times 100$)	BPR (0.07)	BPR (0.03)	BPR (0.01)	MSE ($\times 100$)	BPR (0.07)	BPR (0.03)	BPR (0.01)
Supervised	EPINet [19]	0.431	15.540	42.438	75.800	1.265	6.992	32.292	72.562
	LFAttNet [21]	0.405	10.231	35.711	74.166	0.827	4.206	21.862	67.076
Unsupervised	UnCNN [31]	0.960	20.031	53.104	82.405	4.876	21.944	56.391	84.684
	UnMonocular [32]	0.859	8.783	47.252	82.033	4.551	7.073	21.986	63.595
	Ours	0.643	6.745	24.210	60.513	2.336	5.514	12.937	42.088
Methods		Pinenuts white				Smiling crowd roses			
		MSE ($\times 100$)	BPR (0.07)	BPR (0.03)	BPR (0.01)	MSE ($\times 100$)	BPR (0.07)	BPR (0.03)	BPR (0.01)
Supervised	EPINet [19]	0.509	15.232	35.826	69.557	3.148	14.997	41.297	77.024
	LFAttNet [21]	0.406	10.698	27.042	65.995	2.025	12.454	33.356	66.702
Unsupervised	UnCNN [31]	2.099	35.955	65.235	89.028	5.143	32.653	62.062	86.544
	UnMonocular [32]	0.803	14.146	39.468	74.769	6.257	13.522	28.691	73.238
	Ours	0.434	8.106	25.164	61.817	3.243	11.325	23.254	50.507

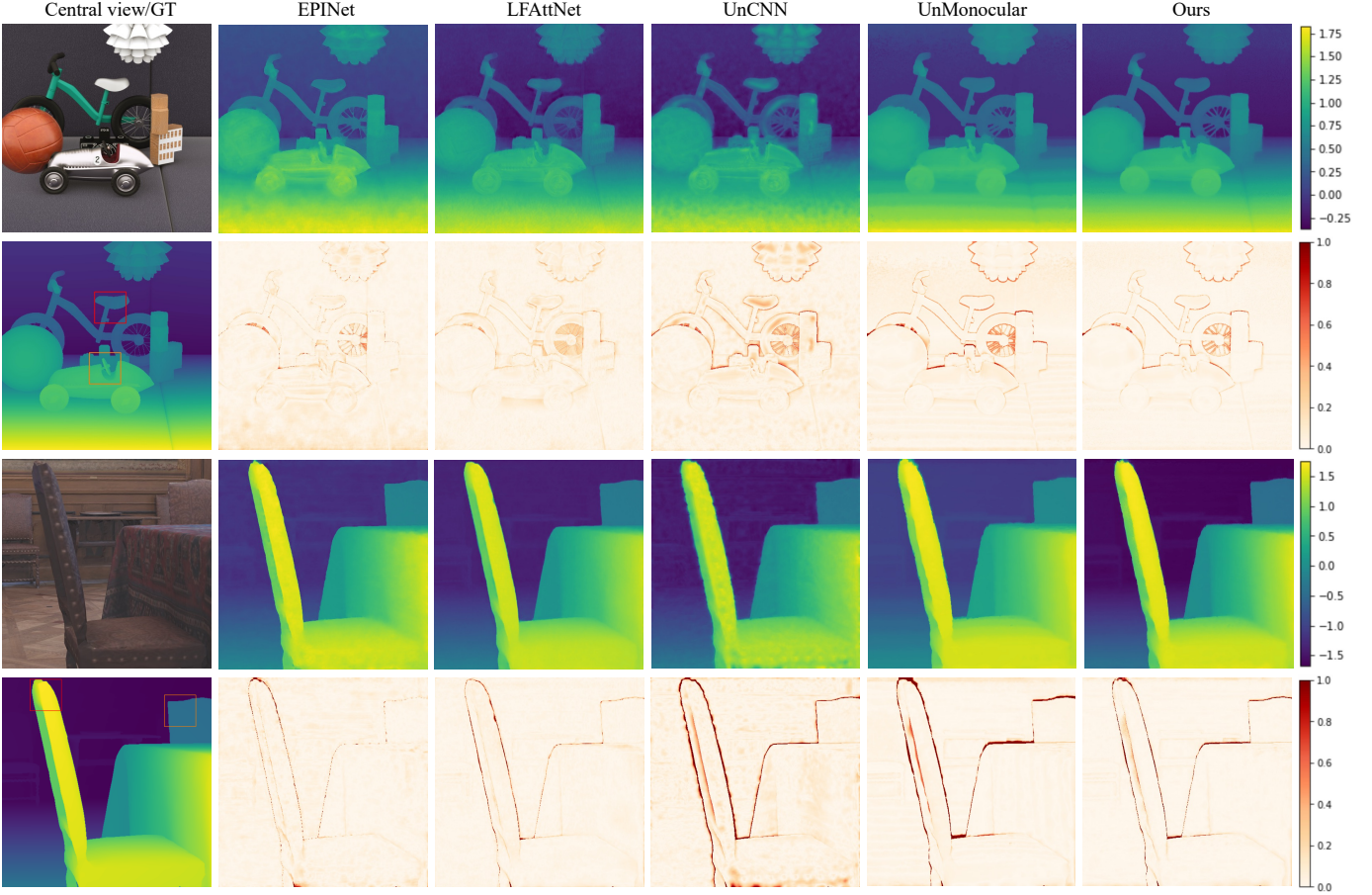


Fig. 6. Visual results of different methods on the scenes from the DLF dataset [20], with the error maps relative to the ground truths.

C. Comparisons

We compared our method with several the other state-of-the-art LF depth estimation methods, including both the supervised and unsupervised methods, on various LF datasets.

1) *Evaluation on the synthetic dense LF images*: First, we recorded the quantitative results of different methods on several scenes from the HCI dataset, as shown in Table I. The metrics for evaluation are the mean square error (MSE) and bad pixel ratios (BPR) [41] with thresholds 0.07, 0.03 and 0.01 (lower is better for all). We compared with two

supervised methods, EPINet [19] and LFAttNet [21], two non-learning-based methods, OCC [26] and FBS [15], and three unsupervised methods, UnCNN [31], UnMonocular [32] and UnOCC [33]. The results of other methods were directly obtained from the benchmark of the HCI dataset [41] or the original paper¹. It can be seen that our method still has some gaps with the supervised methods but can generally outperform the other unsupervised methods. The visual results of some

¹The results of UnOCC [33] are from the original paper, and they only give the MSE and BPR with threshold 0.07.

TABLE III
EVALUATION ON THE SLF DATASET. **RED**: BEST AMONG ALL THE METHODS; **BLUE**: BEST AMONG THE UNSUPERVISED METHODS.

Methods		Lion				Rooster clock			
		MSE	BPR (0.3)	BPR (0.1)	BPR (0.05)	MSE	BPR (0.3)	BPR (0.1)	BPR (0.05)
Supervised	EPINet [19]	0.476	31.457	68.138	82.954	0.740	36.868	71.562	85.147
	LFAttNet [21]	0.372	12.994	29.594	49.327	0.278	6.831	25.813	50.920
Unsupervised	UnCNN [31]	1.442	58.221	84.867	92.373	9.213	34.586	75.021	87.383
	UnMonocular [32]	0.760	48.305	87.371	94.673	0.664	39.931	73.601	86.370
	Ours	0.360	8.766	24.420	47.911	0.261	5.796	25.303	48.668
Methods		Toy bricks				Electro devices			
		MSE	BPR (0.3)	BPR (0.1)	BPR (0.05)	MSE	BPR (0.3)	BPR (0.1)	BPR (0.05)
Supervised	EPINet [19]	1.057	34.658	61.957	77.491	1.112	39.809	64.455	81.793
	LFAttNet [21]	0.738	11.607	29.018	52.576	0.703	13.819	38.731	60.993
Unsupervised	UnCNN [31]	2.254	53.922	82.172	90.950	2.181	41.163	72.970	85.866
	UnMonocular [32]	1.226	47.594	71.098	84.982	2.736	45.612	75.238	87.332
	Ours	0.772	10.048	30.427	55.732	0.842	13.631	36.038	57.880

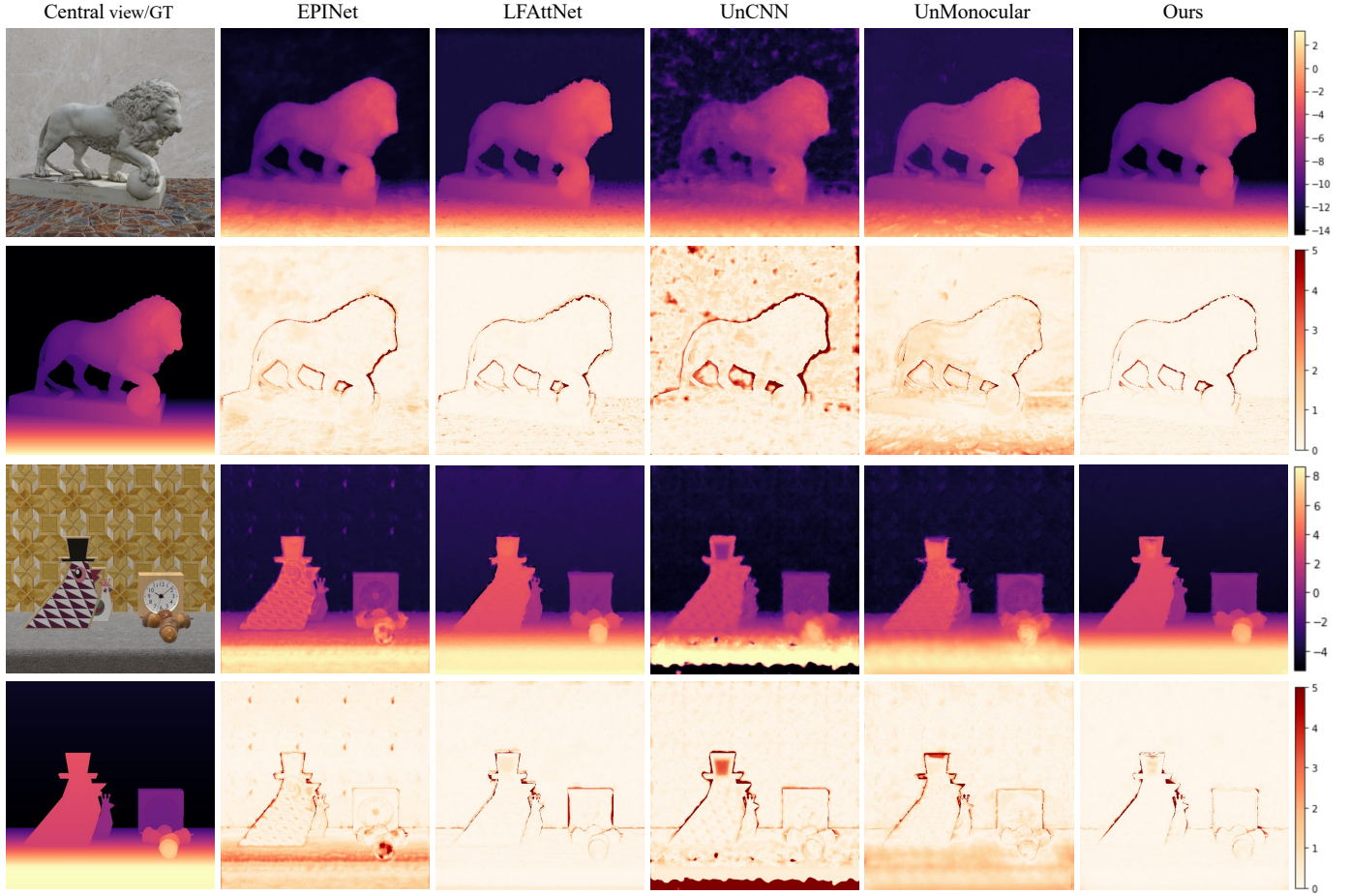


Fig. 7. Visual results of different methods on the sparse LF images from the SLF dataset [20], with the error maps relative to the ground truths.

scenes (Dino and Sideboard), with the error maps relative to the ground truths, are presented in Fig. 5, where we can find that our estimated disparity maps have better visual qualities than the other non-learning-based and unsupervised methods.

Then, we compared the performance of different methods on several scenes from the DLF dataset [20], as recorded in Table II. We re-built the other models, and trained them using the same synthetic dense LF datasets since there are no off-the-shelf models for testing. From our experiments, we can see

that our method obviously outperforms the other unsupervised methods. By comparing with the supervised methods, our method still has some gaps in terms of the MSE, but with lower BPRs. Fig. 6 presents the visual results on the scenes, Toys and Antiques, which reflects that our estimated disparity maps are more visually compelling with proper smoothness and clear object details.

2) *Evaluation on the synthetic sparse LF images:* We also trained these models on the sparse LF images by using the

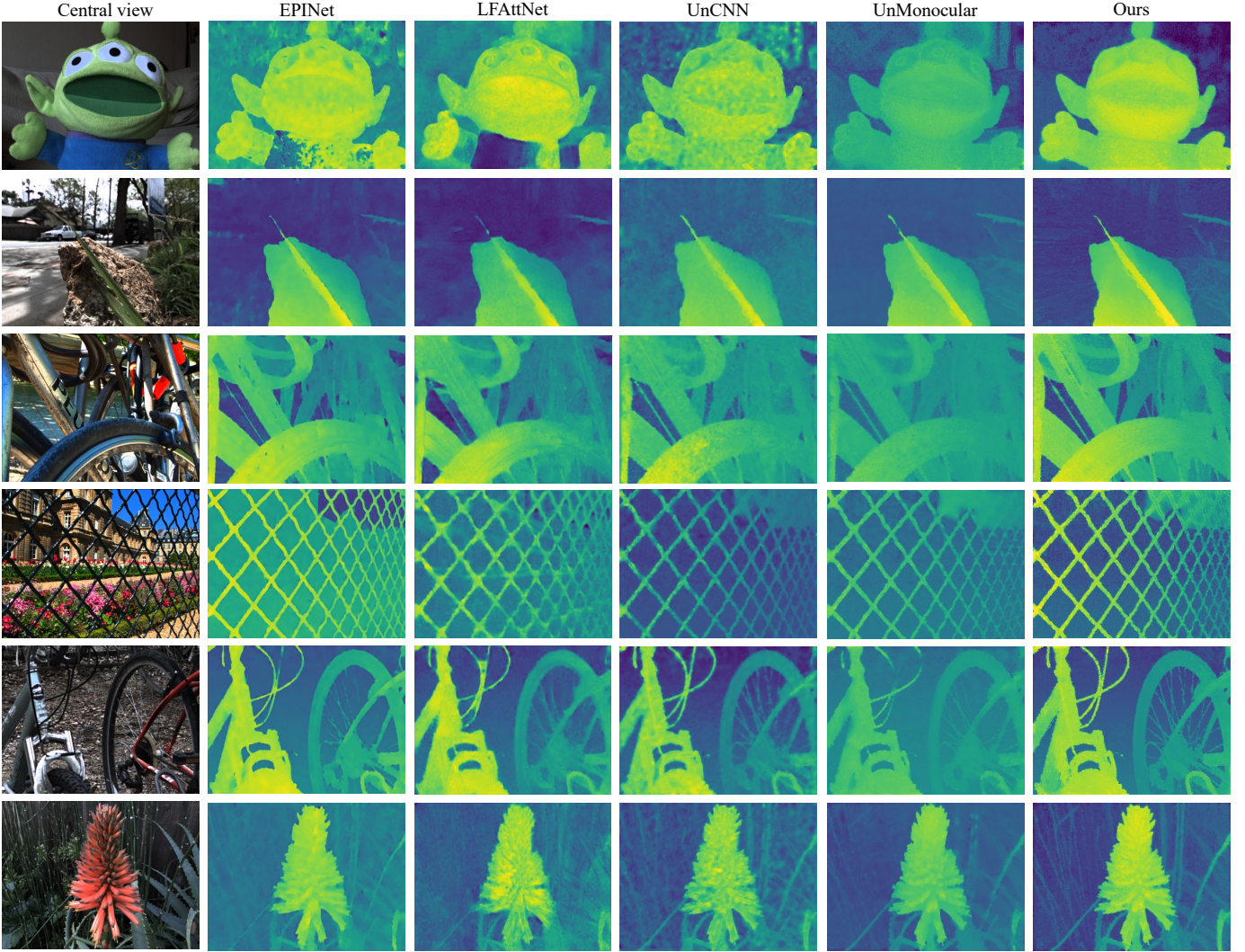


Fig. 8. Visual results of different methods on the real-world LF images from [42]–[44].

SLF dataset [20] and tested them on several scenes. From the quantitative results in Table III, we can find that our method and LFAAttNet [21] have much better results than the others. These two methods both predict the probability distribution of the disparity samples by constructing cost volumes, while the other methods directly output the disparity predictions from the last convolution layer, which increases the difficulty for the networks to learn large disparities. Moreover, our method can achieve comparable quantitative results with the supervised method LFAAttNet [21]. The visual results on the scenes, Lion and Rooster clock, are shown in Fig. 7, with a different color map from dense LFs for distinction. It can be seen that our disparity maps have better visual qualities than the others. However, we can observe that the unsupervised methods have difficulty to estimate disparities in the textureless regions, as depicted in the black areas of Rooster clock. The reason is that it is difficult to match the feature points in these regions since the inaccurate disparities can also lead to correct view reconstruction using the nearby similar pixels.

3) *Evaluation on the real-world LF images:* To evaluate the performance on the real-world scenes, we tested different methods on the real-world LF images from [42]–[44]. All the methods were trained only by the synthetic LF datasets. Fig. 8 presents several predicted disparity maps of different methods. As the real-world scenes do not have ground truths, we can only compare their visual qualities. It can be seen that our method achieves more smooth predictions while preserving better object details compared with the others. The supervised methods do not show advantages on the real-world LF images that contain environmental noises. In contrast, our method demonstrates stronger robustness on various LF images.

D. Ablation studies

1) *Effectiveness of the occlusion prediction:* To validate the effectiveness of our OccNet for occlusion prediction, we trained another model by removing the OccNet and the loss terms ℓ_{rec} and $\ell_{\text{sm-occ}}$ in Eq. 15. Moreover, the pixel-wise weight of the photometric loss in Eq. 10 was reduced to 0.5. We chose several testing samples from the HCI and DLF

TABLE IV
ABLATION STUDY ON THE FRAMEWORK. BOLD: BEST.

Configurations	Parameters	MSE($\times 100$) \downarrow	BPR(0.07) \downarrow	BPR(0.03) \downarrow	BPR(0.01) \downarrow
Ours	1.802 M	2.266	9.238	21.683	54.042
w/o OccNet	1.802 M	2.701	10.806	24.466	58.244
w/o coarse-to-fine	1.799 M	3.057	11.487	27.302	62.725

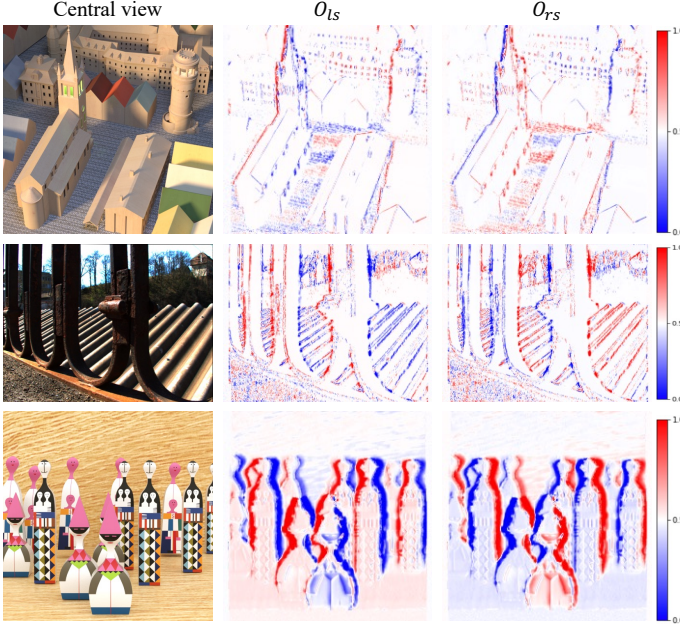


Fig. 9. The predicted occlusion maps of a synthetic dense LF, a real-world LF and a synthetic sparse LF. The red pixels with values approximate to 1 denote larger contributions for the reconstruction of central view and also larger weights for the photometric loss. The case is opposite for the blue pixels with values approximate to 0.

datasets to compare the results of different configurations. The quantitative results are recorded in Table IV, where we can find that the performance is degraded significantly if the OccNet is not employed.

The predicted occlusion maps are presented in Fig. 9, including a synthetic dense LF, a real-world LF and a synthetic sparse LF. The occlusion regions are usually near the object boundaries [46], which leads to the larger or smaller values within these regions in the occlusion maps. The red pixels denote larger contributions for the reconstruction of the central view and also larger weights for the photometric loss. The case is opposite for the blue pixels. Moreover, due to the larger disparity range, the sparse LFs usually have larger occlusion regions, which results in much thicker red and blue regions near the object boundaries compared with the dense LFs.

2) *Effectiveness of the coarse-to-fine structure*: We validated the coarse-to-fine structure in DispNet by training another model without the branch of residual estimation. From Table IV, we can see that the quantitative results have an obvious decline if the coarse-to-fine structure is not adopted, which indicates that the refinement branch with finer interval samplings can significantly improve the disparity

accuracy. Moreover, the refinement branch only introduces extra 0.003 M parameters since the feature extractor and the cost filters are all shared by the two branches.

TABLE V
ABLATION STUDY ON THE LOSS TERMS. BOLD: BEST.

Settings	MSE($\times 100$) \downarrow	BPR(0.07) \downarrow	BPR(0.03) \downarrow	BPR(0.01) \downarrow
Full loss	2.266	9.238	21.683	54.042
w/o ℓ_{sm}	2.457	9.749	22.136	55.856
w/o ℓ_{SSIM}	2.393	9.535	22.027	55.250

3) *Effectiveness of the loss terms*: We trained extra models by excluding the smoothness loss and SSIM loss, respectively. Table V lists the corresponding results, which suggests that the MSE and BPRs slightly increase after removing the smoothness loss or SSIM loss. Therefore, these two loss terms can contribute to a better performance.

TABLE VI
ABLATION STUDY ON THE DISPARITY FUSION APPROACHES. BOLD: BEST.

Settings	MSE($\times 100$) \downarrow	BPR(0.07) \downarrow	BPR(0.03) \downarrow	BPR(0.01) \downarrow
Weighted fusion ($n' = 2$)	2.266	9.238	21.683	54.042
Weighted fusion ($n' = 4$)	2.564	10.022	22.513	54.462
Minimum error fusion	2.411	10.210	23.743	57.842
w/o occlusion handling	2.837	10.371	23.441	56.778

4) *Effectiveness of the disparity fusion strategy*: We also validated our disparity fusion strategy, and our default approach is the weighted fusion by using two disparities ($n' = 2$) with the smallest errors at each position. The other fusion approaches include the weighted fusion by using all the disparities ($n' = 4$) and the minimum error fusion that selects the disparity with the minimum error at each position. Their performances are recorded in Table VI, where we can observe that the MSE increases obviously if the weighted fusion with all the disparities is used, and the BPRs increase obviously if the minimum error fusion is used. If occlusions are not considered when deriving the error maps, the estimated error of each position is represented only by the mean of all the warping errors. The corresponding results ('w/o occlusion handling') suggest that the performance is degraded significantly if occlusions are not handled during fusion.

Fig. 10 gives an example of disparity fusion performance, including four estimated disparity maps from the two horizontal and two vertical input combinations, and the final disparity map derived by the weighted fusion according to Eq. 21. It can be seen that the final disparity map has smaller errors and better visual quality by merging good pixels from the individual disparity maps.

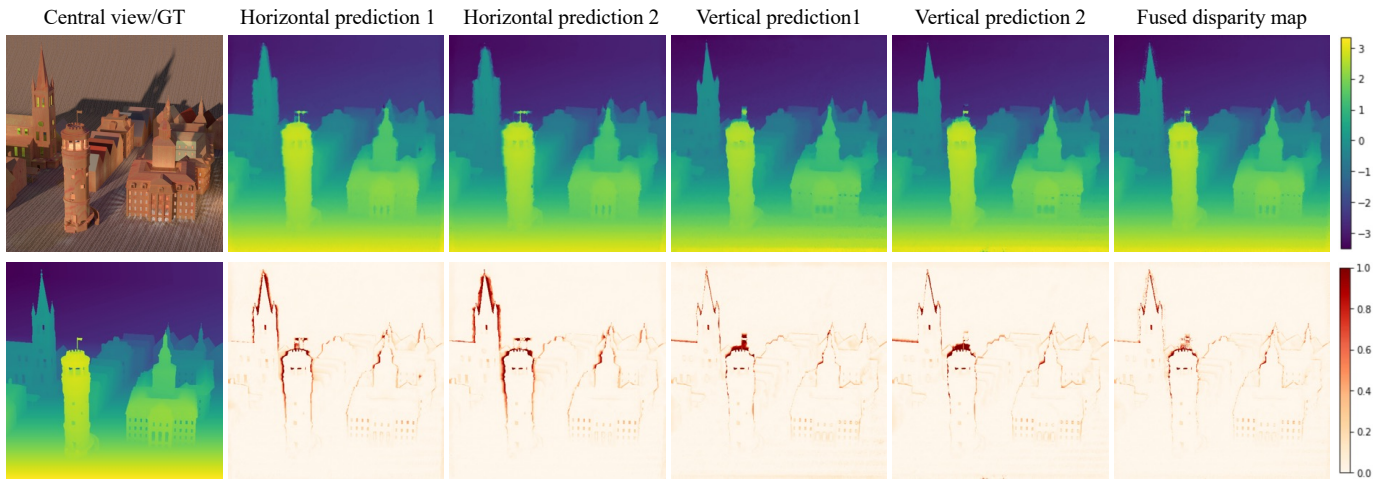


Fig. 10. The disparity maps estimated from two horizontal and two vertical input combinations, and the final disparity map after weighted fusion. The second row shows the error maps of the corresponding predictions relative to the ground truths.

V. CONCLUSION

In this paper, we propose an unsupervised framework for LF depth estimation. We design a DispNet that takes as inputs multiple view combinations to predict disparity maps in different ranges. Our DispNet adopts a coarse-to-fine structure with two branches to estimate the coarse and residual disparity maps, respectively, by performing multi-view feature matching. Photo-consistency is the main supervisory signal for the training without ground truths. However, it does not hold anymore in the occlusion regions. Thus, we introduce an OccNet to predict the occlusion maps, which are used as the element-wise weights of the photometric loss to alleviate the impact of occlusions on the disparity learning. The OccNet is trained by the reconstruction loss with no label required. The multiple estimated disparity maps after rotating and scaling are fused based on their estimated errors using the diagonal views with effective occlusion handling to obtain the final disparity map. Our framework achieves superior performance on both the dense and sparse LF images, and also shows better generalization ability to the real-world LF images.

ACKNOWLEDGMENT

The work is supported in part by the Research Grants Council of Hong Kong (GRF 17200019, 17201620, 17200321) and by ACCESS — AI Chip Center for Emerging Smart Systems, Hong Kong SAR.

REFERENCES

- [1] R. Ng, M. Levoy, M. Brédif, G. Duval, M. Horowitz, and P. Hanrahan, "Light field photography with a hand-held plenoptic camera," *Computer Science Technical Report*, vol. 2, no. 11, pp. 1–11, 2005.
- [2] E. Y. Lam, "Computational photography with plenoptic camera and light field capture: tutorial," *Journal of the Optical Society of America A*, vol. 32, no. 11, pp. 2021–2032, 2015.
- [3] S. Zhang, N. Meng, and E. Y. Lam, "LRT: An efficient low-light restoration transformer for dark light field images," *arXiv preprint*, 2022.
- [4] C. Kim, H. Zimmer, Y. Pritch, A. Sorkine-Hornung, and M. H. Gross, "Scene reconstruction from high spatio-angular resolution light field," *ACM Transactions on Graphics*, vol. 32, no. 4, 2013.
- [5] Z. Cai, X. Liu, X. Peng, Y. Yin, A. Li, J. Wu, and B. Z. Gao, "Structured light field 3d imaging," *Optics Express*, vol. 24, no. 18, pp. 20324–20334, 2016.
- [6] J. Jin, J. Hou, H. Yuan, and S. Kwong, "Learning light field angular super-resolution via a geometry-aware network," in *AAAI Conference on Artificial Intelligence*, 2020, pp. 11 141–11 148.
- [7] C. Zhu, H. Zhang, W. Chen, M. Tan, and Q. Liu, "An occlusion compensation learning framework for improving the rendering quality of light field," *IEEE Transactions on Neural Networks and Learning Systems*, vol. 32, no. 12, pp. 5738–5752, 2021.
- [8] M. Suhail, C. Esteves, L. Sigal, and A. Makadia, "Light field neural rendering," in *IEEE/CVF Conference on Computer Vision and Pattern Recognition (CVPR)*, 2022, pp. 8269–8279.
- [9] S. Wanner and B. Goldluecke, "Variational light field analysis for disparity estimation and super-resolution," *IEEE Transactions on Pattern Analysis and Machine Intelligence*, vol. 36, no. 3, pp. 606–619, 2014.
- [10] S. Zhang, H. Sheng, C. Li, J. Zhang, and Z. Xiong, "Robust depth estimation for light field via spinning parallelogram operator," *Computer Vision and Image Understanding*, vol. 145, pp. 148–159, 2016.
- [11] Y. Zhang, H. Lv, Y. Liu, H. Wang, X. Wang, Q. Huang, X. Xiang, and Q. Dai, "Light-field depth estimation via epipolar plane image analysis and locally linear embedding," *IEEE Transactions on Circuits and Systems for Video Technology*, vol. 27, no. 4, pp. 739–747, 2017.
- [12] H. Sheng, P. Zhao, S. Zhang, J. Zhang, and D. Yang, "Occlusion-aware depth estimation for light field using multi-orientation EPIS," *Pattern Recognition*, vol. 74, pp. 587–599, 2018.
- [13] H.-G. Jeon, J. Park, G. Choe, J. Park, Y. Bok, Y.-W. Tai, and I. So Kweon, "Accurate depth map estimation from a lenslet light field camera," in *IEEE Conference on Computer Vision and Pattern Recognition (CVPR)*, 2015.
- [14] M. W. Tao, P. P. Srinivasan, J. Malik, S. Rusinkiewicz, and R. Ramamoorthi, "Depth from shading, defocus, and correspondence using light-field angular coherence," in *IEEE Conference on Computer Vision and Pattern Recognition (CVPR)*, 2015.
- [15] J. Y. Lee and R.-H. Park, "Depth estimation from light field by accumulating binary maps based on foreground-background separation," *IEEE Journal of Selected Topics in Signal Processing*, vol. 11, no. 7, pp. 955–964, 2017.
- [16] C.-T. Huang, "Empirical bayesian light-field stereo matching by robust pseudo random field modeling," *IEEE Transactions on Pattern Analysis and Machine Intelligence*, vol. 41, no. 3, pp. 552–565, 2019.
- [17] X. Sun, Z. Xu, N. Meng, E. Y. Lam, and H. K.-H. So, "Data-driven light field depth estimation using deep convolutional neural networks," in *International Joint Conference on Neural Networks (IJCNN)*, 2016, pp. 367–374.
- [18] S. Heber, W. Yu, and T. Pock, "Neural EPI-volume networks for shape from light field," in *IEEE International Conference on Computer Vision (ICCV)*, 2017.
- [19] C. Shin, H.-G. Jeon, Y. Yoon, I. S. Kweon, and S. J. Kim, "EPINET: A fully-convolutional neural network using epipolar geometry for depth

- from light field images,” in *IEEE Conference on Computer Vision and Pattern Recognition (CVPR)*, 2018.
- [20] J. Shi, X. Jiang, and C. Guillemot, “A framework for learning depth from a flexible subset of dense and sparse light field views,” *IEEE Transactions on Image Processing*, vol. 28, no. 12, pp. 5867–5880, 2019.
- [21] Y.-J. Tsai, Y.-L. Liu, M. Ouhyoung, and Y.-Y. Chuang, “Attention-based view selection networks for light-field disparity estimation,” in *AAAI Conference on Artificial Intelligence*, 2020.
- [22] J. Chen, S. Zhang, and Y. Lin, “Attention-based multi-level fusion network for light field depth estimation,” in *AAAI Conference on Artificial Intelligence*, 2021.
- [23] T. Zhou, M. Brown, N. Snavely, and D. G. Lowe, “Unsupervised learning of depth and ego-motion from video,” in *IEEE Conference on Computer Vision and Pattern Recognition (CVPR)*, 2017.
- [24] Q. Sun, Y. Tang, C. Zhang, C. Zhao, F. Qian, and J. Kurths, “Unsupervised estimation of monocular depth and vo in dynamic environments via hybrid masks,” *IEEE Transactions on Neural Networks and Learning Systems*, pp. 1–11, 2021.
- [25] C. Zhao, G. G. Yen, Q. Sun, C. Zhang, and Y. Tang, “Masked gan for unsupervised depth and pose prediction with scale consistency,” *IEEE Transactions on Neural Networks and Learning Systems*, vol. 32, no. 12, pp. 5392–5403, 2021.
- [26] T.-C. Wang, A. A. Efros, and R. Ramamoorthi, “Depth estimation with occlusion modeling using light-field cameras,” *IEEE Transactions on Pattern Analysis and Machine Intelligence*, vol. 38, no. 11, pp. 2170–2181, 2016.
- [27] W. Williem and I. K. Park, “Robust light field depth estimation for noisy scene with occlusion,” in *IEEE Conference on Computer Vision and Pattern Recognition (CVPR)*, 2016.
- [28] J. Chen, J. Hou, Y. Ni, and L.-P. Chau, “Accurate light field depth estimation with superpixel regularization over partially occluded regions,” *IEEE Transactions on Image Processing*, vol. 27, no. 10, pp. 4889–4900, 2018.
- [29] E. Ilg, N. Mayer, T. Saikia, M. Keuper, A. Dosovitskiy, and T. Brox, “FlowNet 2.0: Evolution of optical flow estimation with deep networks,” in *IEEE Conference on Computer Vision and Pattern Recognition (CVPR)*, 2017.
- [30] P. P. Srinivasan, T. Wang, A. Sreelal, R. Ramamoorthi, and R. Ng, “Learning to synthesize a 4d rgbd light field from a single image,” in *IEEE International Conference on Computer Vision (ICCV)*, 2017.
- [31] J. Peng, Z. Xiong, D. Liu, and X. Chen, “Unsupervised depth estimation from light field using a convolutional neural network,” in *International Conference on 3D Vision*, 2018, pp. 295–303.
- [32] W. Zhou, E. Zhou, G. Liu, L. Lin, and A. Lumsdaine, “Unsupervised monocular depth estimation from light field image,” *IEEE Transactions on Image Processing*, vol. 29, pp. 1606–1617, 2020.
- [33] J. Jin and J. Hou, “Occlusion-aware unsupervised learning of depth from 4-d light fields,” *IEEE Transactions on Image Processing*, vol. 31, pp. 2216–2228, 2022.
- [34] L.-C. Chen, G. Papandreou, F. Schroff, and H. Adam, “Rethinking atrous convolution for semantic image segmentation,” *arXiv preprint*, 2017.
- [35] J.-R. Chang and Y.-S. Chen, “Pyramid stereo matching network,” in *IEEE Conference on Computer Vision and Pattern Recognition (CVPR)*, 2018.
- [36] Z. Rao, Y. Dai, Z. Shen, and R. He, “Rethinking training strategy in stereo matching,” *IEEE Transactions on Neural Networks and Learning Systems*, pp. 1–14, 2022.
- [37] A. Kendall, H. Martirosyan, S. Dasgupta, P. Henry, R. Kennedy, A. Bachrach, and A. Bry, “End-to-end learning of geometry and context for deep stereo regression,” in *IEEE International Conference on Computer Vision (ICCV)*, 2017.
- [38] Z. Wang, A. C. Bovik, H. R. Sheikh, and E. P. Simoncelli, “Image quality assessment: from error visibility to structural similarity,” *IEEE Transactions on Image Processing*, vol. 13, no. 4, pp. 600–612, 2004.
- [39] A. Ranjan, V. Jampani, L. Balles, K. Kim, D. Sun, J. Wulff, and M. J. Black, “Competitive collaboration: Joint unsupervised learning of depth, camera motion, optical flow and motion segmentation,” in *IEEE/CVF Conference on Computer Vision and Pattern Recognition (CVPR)*, 2019.
- [40] S. Zhang and E. Y. Lam, “An effective decomposition-enhancement method to restore light field images captured in the dark,” *Signal Processing*, vol. 189, p. 108279, 2021.
- [41] K. Honauer, O. Johannsen, D. Kondermann, and B. Goldluecke, “A Dataset and Evaluation Methodology for Depth Estimation on 4D Light Fields,” in *Asian Conference on Computer Vision*, 2016, pp. 19–34.
- [42] R. Shah, G. Wetzstein, A. S. Raj, and M. Lowney, “Stanford lytro light field archive,” 2016.
- [43] N. K. Kalantari, T. C. Wang, and R. Ramamoorthi, “Learning-based view synthesis for light field cameras,” *ACM Transactions on Graphics*, vol. 35, no. 6, 2016.
- [44] M. Rerabek and T. Ebrahimi, “New light field image dataset,” in *International Conference on Quality of Multimedia Experience*, 2016.
- [45] D. P. Kingma and J. Ba, “Adam: A method for stochastic optimization,” in *International Conference on Learning Representations (ICLR)*, 2015.
- [46] N. Meng, K. Li, J. Liu, and E. Y. Lam, “Light field view synthesis via aperture disparity and warping confidence map,” *IEEE Transactions on Image Processing*, vol. 30, pp. 3908–3921, 2021.